

Article

A Phantom Investigation to Quantify Huygens Principle Based Microwave Imaging for Bone Lesion Detection

Banafsheh Khalesi ^{1,*}, Behnaz Sohani ¹, Navid Ghavami ², Mohammad Ghavami ¹, Sandra Dudley ¹ and Gianluigi Tiberi ¹

¹ School of Engineering, London South Bank University, London SE1 0AA, UK; sohanib@lsbu.ac.uk (B.S.); ghavamim@lsbu.ac.uk (M.G.); dudleyms@lsbu.ac.uk (S.D.); g.tiberi@iet.unipi.it (G.T.)

² UBT-Umbria Bioengineering Technologies, Spin off of University of Perugia, 06081 Assisi, Italy; navgh1988@yahoo.co.uk

* Correspondence: khalesib@lsbu.ac.uk

Received: 4 November 2019; Accepted: 3 December 2019; Published: 9 December 2019



Abstract: This paper demonstrates the outcomes of a feasibility study of a microwave imaging procedure based on the Huygens principle for bone lesion detection. This study has been performed using a dedicated phantom and validated through measurements in the frequency range of 1–3 GHz using one receiving and one transmitting antenna in free space. Specifically, a multilayered bone phantom, which is comprised of cortical bone and bone marrow layers, was fabricated. The identification of the lesion's presence in different bone layers was performed on images that were derived after processing through Huygens' principle, the S21 signals measured inside an anechoic chamber in multi-bistatic fashion. The quantification of the obtained images was carried out by introducing parameters such as the resolution and signal-to-clutter ratio (SCR). The impact of different frequencies and bandwidths (in the 1–3 GHz range) in lesion detection was investigated. The findings showed that the frequency range of 1.5–2.5 GHz offered the best resolution (1.1 cm) and SCR (2.22 on a linear scale). Subtraction between S21 obtained using two slightly displaced transmitting positions was employed to remove the artefacts; the best artefact removal was obtained when the spatial displacement was approximately of the same magnitude as the dimension of the lesion.

Keywords: microwave imaging; phantom measurement system; bone lesion detection

1. Introduction

Bone fracture can be caused as a result of high force impact, a simple accident, stress or certain medical conditions that weaken the bones. The structure of the bones includes two principle parts: (i) cortical (compact) bone, which is a hard outer layer and is dense, strong, durable and surrounded by the cancellous tissue, and (ii) bone marrow, which is the inner layer, less dense and with a lighter content. There are many types of bone fractures [1]. Depending on the fracture severity, the injuries can lead to a reduction in the mobility of the patient [2]. X-rays, computed tomography (CT) and magnetic resonance imaging (MRI) are used as essential tools in the diagnosis and monitoring of bone conditions, including fractures, and joint abnormalities [3]. However, each technique suffers from its own negative aspects. For instance, fractures can be commonly detected by X-rays [4], which is the fastest and easiest way to assess bone injuries, including fractures. However, since this technique involves radiation and can potentially cause damage, it raises major concerns especially in the cases of infants and stages of pregnancy. In addition, X-rays provide limited information about muscles, tendons or joints [5]. Nevertheless, CT is very effective for imaging and gives better quality images for body organs, such as an image of complicated fractures, subtle fractures or dislocations. However, similar to X-rays, ionizing

radiation is the major problem of using this technique, which leads to limits in its application [6]. There is no ionizing radiation in the MRI technique, and it may be more useful in identifying bone and joint injuries. MRI can also detect occult fractures or bone bruises that are not visible on X-ray images, but the high cost of purchasing and maintaining such systems and their long time duration cause financial restrictions. Moreover, none of these devices are portable and cannot be used at the accident site. Thus, a fast and portable imaging system could be particularly useful locally for rapid diagnosis of bone injuries. A wide range of research concentrates on the development of new medical imaging techniques to achieve a portable, low cost and safe imaging alternative. Among these, using microwave imaging techniques has attracted the attention of researchers due to its various benefits such as the use of non-ionizing signals, low cost, low complexity and its ability to penetrate through different mediums (air, skin, bones and tissues [7]). The dielectric properties of human tissues can be used as an effective and accurate indicator for diagnostic purposes [8]. The significant difference between the dielectric properties of tissues with lesion and healthy tissues of the human body at microwave frequencies is the basis of microwave medical imaging techniques. Microwave tomography techniques, which give the maps of dielectric properties [9–11], and the UWB radar techniques, which aim to find and locate the significant scatterers [11–14], are recognized as the two main branches of microwave imaging techniques [14]. Nevertheless, microwave tomography has its drawbacks such as low signal-to-clutter and complex mathematical formulation. Both microwave tomography and UWB radar techniques have been increasingly well investigated for stroke detection [15], breast cancer detection [16], bone imaging [17,18], and skin cancer detection [19] through using different approaches at different frequency ranges.

UWB imaging for bone lesion detection has been studied through using matching liquids [17,18]. We propose imaging execution using two antennas operating in free space. Imaging was performed via a Huygens principle (HP) based algorithm, which was initiated originally for breast imaging. Explicitly, S_{21} signals in the frequency range 1–3 GHz [18] were collected in a multi-bistatic fashion in an anechoic chamber setting using a multilayer phantom, mimicking bones. A realistic multilayer bone mimicking phantom comprised of cortical bone mimicking and bone marrow mimicking layers was constructed. Subsequently, a large inclusion was placed within the marrow layer to represent bone marrow lesion, and afterwards, a small inclusion was placed in the cortical layer to represent the bone lesion or fracture. Angular subtraction rotation was used for artefact removal, allowing lesion detection.

Additionally, quantification of the images obtained through HP microwave imaging was performed by introducing dedicated parameters such as the resolution and signal-to-clutter ratio. Furthermore, investigating the impact of different frequencies and bandwidths, lesion size and angular rotation subtraction in the detection procedure were also addressed.

This paper is organized as follows. The phantom construction procedure, the experimental setup used for phantom measurements, the imaging procedure and image quantification are described in Section 2. Section 3 represents the corresponding experimental results and discussions. Finally, conclusions are presented in Section 4.

2. Materials and Methods

2.1. Phantom Construction

This section presents the design and fabrication of a multilayered cylindrical phantom mimicking the human bone by considering the relative permittivity and conductivity with the aim of performing microwave imaging experiments in the frequency range of 1 to 3 GHz. Hence, our proposed multilayered bone phantom was comprised of two layers, which included: (i) an external layer representing the cortical bone tissue (radius = 5.5 cm) and (ii) an internal layer representing the bone marrow tissue (radius = 3.5 cm). A small size inclusion (radius = 0.3 cm) was placed in the cortical bone layer to represent the bone fracture, and a larger sized inclusion (radius = 0.7 cm) was placed in

the bone marrow layer to represent the internal bone lesion. In this paper, the lesion was assumed to have the dielectric properties of blood.

The phantom fabrication procedure for each layer of phantom was performed by considering the following factors: (i) dielectric property (permittivity and conductivity) similarity of the layers with the tissues to be mimicked, (ii) an easy construction process, (iii) the stability of the materials and (iv) the geometric dimension similarity between each layer and the realistic scenario. The upper half of Table 1 shows the dielectric properties of each tissue to be mimicked, where the values were derived from [20], while the lower half of the Table indicates the dielectric properties of the tissue mimicking materials used.

Table 1. Relative permittivity and conductivity at a frequency of 2 GHz.

	Relative Permittivity	Conductivity (S/m)
Bone marrow	5.35	0.07
Bone cortical	11.7	0.31
Lesion (assumed here as blood)	59	2.19
Bone marrow tissue equivalent material (ZMT Zurich MedTech Company, TLec24 oil)	5	0.2
Bone cortical tissue equivalent material (ZMT Zurich MedTech Company, TLe11.5c.045 oil)	7	0.3
Blood tissue equivalent material (40% glycerol and 60% water)	60	2

To construct the multilayered bone phantom appropriately, different volumes of cylindrically shaped plastic containers and tubes were used and are shown in Figure 1.



Figure 1. Design of the different layers of the phantom.

As shown in Table 2, the phantom fabrication was performed using a large cylindrically shaped plastic container with a radius of 5.5 cm and a height of 13 cm filled with cortical bone equivalent material to represent the cortical bone layer. Then, a medium sized cylindrically shaped plastic container with a radius of 3.5 cm and a height of 9 cm was placed inside the large container after filling it up with bone marrow equivalent material representing the bone marrow layer. Subsequently, the small cylindrically shaped plastic tube with radius = 0.3 cm and a height of 13 cm filled up with lesion equivalent material was placed inside the cortical bone layer to represent bone fracture (see Figure 2a). In the next scenario, the larger cylindrically shaped plastic tube having a radius equal to 0.7 cm and a height equal to 11 cm, again filled up with lesion equivalent material, was placed inside the bone marrow layer to represent bone marrow lesion (see Figure 2b).

Table 2. Phantom layers' design height and size.

Different Layers of the Phantom	Radius (cm)	Height (cm)
Bone marrow (internal layer)	3.5	9
Bone cortical (external layer)	5.5	13
Small lesion	0.3	13
Large lesion	0.7	11

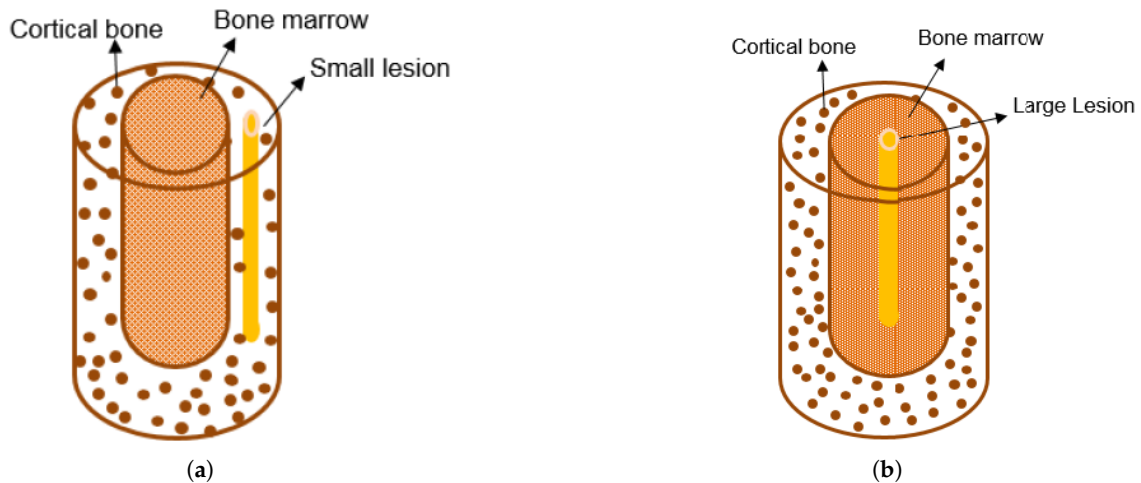


Figure 2. Design of the proposed bone fracture (a) and bone marrow lesion (b).

Different recipes for each layer of the phantom were tested to select those showing dielectric properties similar to those given in the upper half of Table 1. In this context, dedicated liquids were purchased from the ZMT Zurich MedTech Company [21]. As shown in the lower half of Table 1, the TLe11.5C.045 oil displayed (at 2 GHz) a dielectric permittivity of 7 and a conductivity of 0.3 S/m; the TLe5C24 displayed (at 2 GHz) a dielectric permittivity of 5 and a conductivity of 0.2 S/m. Thus, TLe11.5C.045 was selected as a cortical bone tissue equivalent material and TLe5C24 as a bone marrow tissue equivalent material. In addition, a mixture of glycerol and water with a ratio of 40% and 60%, respectively, was chosen as the recipe mimicking the lesion (blood), giving (at 2 GHz) a permittivity value equal to 60 and conductivity of 2 S/m [22]. Figure 3a,b shows the fabricated multilayered bone fracture and bone marrow lesion, respectively.

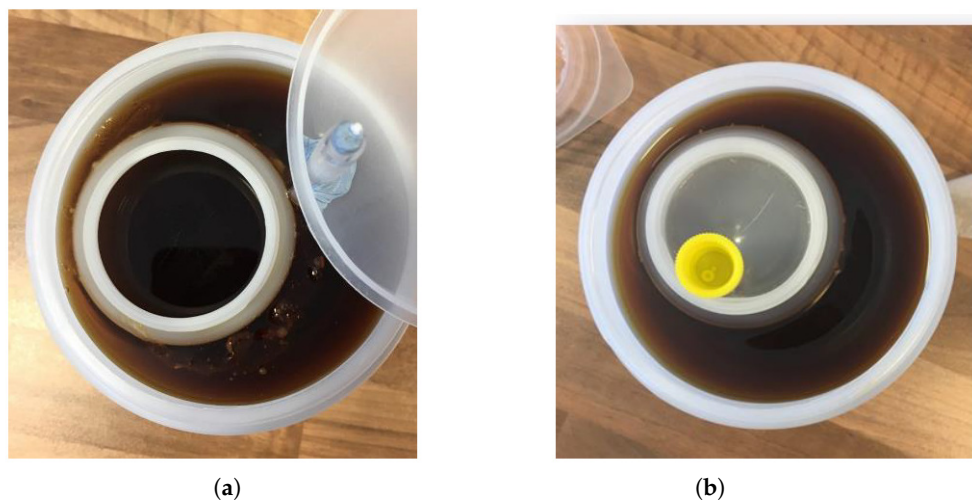


Figure 3. Fabricated bone fracture phantom (a) and bone marrow lesion phantom (b).

2.2. Experimental Configurations in an Anechoic Chamber

All microwave images presented in this paper were obtained by processing the frequency domain measurements obtained in the band of 1 to 3 GHz. Measurements were performed inside an anechoic chamber using a vector network analyser (VNA) (model MS2028C, Anritsu) and PulsON P200 antennas. Specifically, the measurement setup was comprised of one transmitting antenna and one receiving antenna connected to the VNA device. The phantom was placed at the centre of a rotatable table. Transmitting antenna was located 12 cm away from the centre of the table, while the receiving antenna was placed nearer to the object (i.e., 8.5 cm from the centre of the table). Both receiving and transmitting antennas were vertically polarized and omni-directional in the azimuth plane and were calibrated and operated in free space.

The receiving antenna was configured to rotate azimuthally around the phantom to collect the reflected signals in the different directions. For each receiving position, the complex S_{21} was recorded over a wide frequency range of 1 to 3 GHz with a frequency step of 10 MHz [23] in order to exploit the variation of the signal over the different frequencies. To allow artefact removal, the measurement procedure was repeated using $M = 3$ transmitting positions displaced 5° from each other (considered as a transmitting triplet displaced at positions 0° , 5° , and 10°). It should be pointed out that the 3 transmitting positions were synthesized by appropriately rotating the phantom instead of rotating the transmitting antenna. For each transmitting position, the receiving antenna rotated to measure the receiving signal every 6° , which led to a total of $N_{PT} = 60$ receiving points. Figure 4 shows the measurement setup of the multilayered bone phantom inside the anechoic chamber.



Figure 4. Position of the bone marrow lesion phantom inside the anechoic chamber. The phantom was placed in the centre of a rotatable table. The external PulsON P200 antenna is the transmitter, and the internal PulsON P200 antenna is the receiver.

The positions of the phantoms with respect to the transmitting antenna are shown in Figure 5a,b, which represents the pictorial views of the measurement setup.

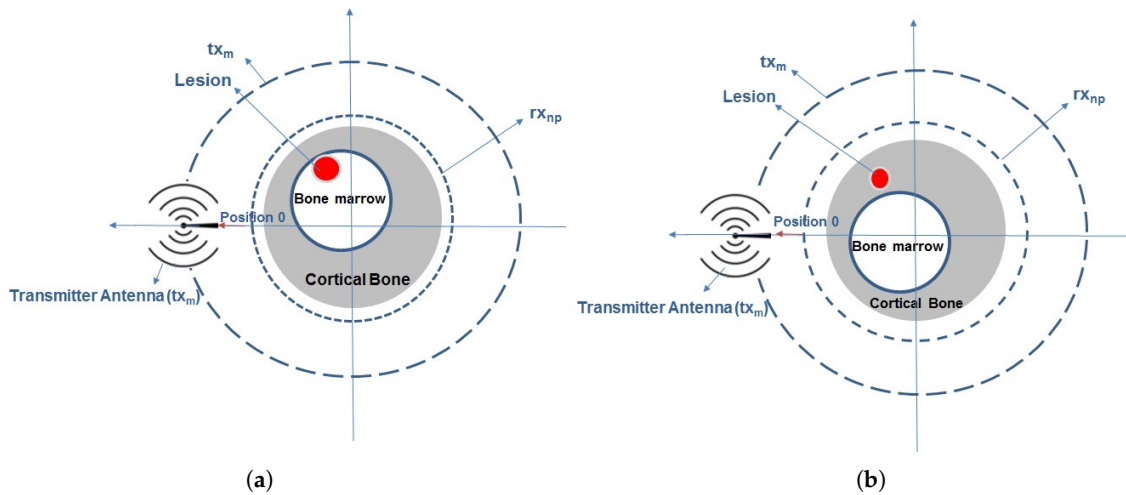


Figure 5. Pictorial view of bone marrow lesion (a) and bone fracture lesion (b) measurement setups.

2.3. Imaging Procedure and Image Quantification

In order to reconstruct the image, the complex measured S_{21} was processed through the Huygens principle [24]. Specifically, the cylindrically shaped object (the phantom) was placed in free space and illuminated by a transmitting antenna located at the position tx_m . The receiving antenna rotated around it to measure the signals at the point $rx_{np} \equiv (a_0, \phi_{np}) \equiv \vec{\rho}_{np}$ displaced along a circular surface having radius a_0 (see Figure 5):

$$S_{21}^{known}_{tx_m} |_{rx_{np}} = S_{21}^{known}_{np,tx_m} \quad \text{with} \quad np = 1, \dots, N_{PT} \quad (np = 1, 2, \dots, 60) \quad (1)$$

where rx_{np} is the position of the receiving antenna, np is the number of receiving point, which varies from 1 to $N_{PT} = 60$, and m represents the transmitting position with $m = 1, 2, 3$.

According to HP: “Each locus of a wave excites the local matter which re-radiates secondary wavelets, and all wavelets superpose to a new, resulting wave (the envelope of those wavelets), and so on” [25]; the field inside the object can be calculated as the superposition of the fields radiated by the N_{PT} receiving points of Equation (1):

$$E_{HP,2D}^{rcstr}(\rho, \phi; tx_m; f) = \Delta s \sum_{np=1}^{N_{PT}} S_{21}^{known}_{np,tx_m} G(k_1 |\vec{\rho}_{np} - \vec{\rho}|) \quad (2)$$

In Equation (2), $(\rho, \phi) \equiv \vec{\rho}$ is the observation point, f is the frequency, k_1 indicates the wave number and Δs is the spatial sampling. The “reconstructed” internal field is indicated by the string “rcstr”, while the string HP indicates that the Huygens based procedure will be employed in Equation (2). In order to propagate the field (since we are dealing with a 3D problem), Green’s function G for homogeneous problems was used [24].

It was shown in [24,26] that Equation (2) can capture the contrast, i.e., mismatch boundaries, and locate an inclusion within the volume.

In Equation (2), k_1 can be set to represent the wave number for the media constituting the external layer (if known). However, it has been shown that detection can be achieved also if setting k_1 as the free space wave number [27].

By the assumption of using N_F frequencies f_i , the intensity of the final image I was obtained through Equation (3), i.e., by summing incoherently all the solutions.

$$I(\rho, \phi; tx_m) = \sum_{i=1}^{N_F} |E_{HP,2D}^{rcstr}(\rho, \phi; tx_m; f_i)|^2 \quad (3)$$

As Equation (4) shows, the subtraction between S21 obtained using two slightly displaced transmitting position was employed in order to remove the artefacts, i.e., the image of the transmitter and the reflection of the first layers [26]:

$$E_{\text{HP,2D}}^{\text{rcstr}}(\rho, \phi; \text{tx}_m - \text{tx}_{m'}; f) = \Delta s \sum_{np=1}^{N_{PT}} \left((S21_{np, \text{tx}_m}^{\text{known}} - S21_{np, \text{tx}_{m'}}^{\text{known}}) G(k_1 |\vec{\rho}_{np} - \vec{\rho}'|) \right) \quad (4)$$

with tx_m and $\text{tx}_{m'}$ belonging to the transmitting triplet. This procedure will be referred to as rotation subtraction artefact removal.

Image Quantification

Images may contain some clutter even following artefact removal procedures. Thus, it is appropriate to introduce some parameters in order to compare and quantify the performance of microwave imaging. The parameters that will be introduced are the resolution and signal-to-clutter ratio (SCR). Specifically, here, the resolution is defined as a dimension of the region whose normalized intensity is above 0.5 [28]; SCR was defined as the ratio between maximum intensity evaluated in the region of the lesion divided by the maximum intensity outside the region of the lesion [29]. The evaluation of these parameters was performed for both external and internal lesion placement in the two following scenarios: (i) calculating Equation (3) maintaining the same bandwidth of 0.5 GHz and varying the central frequency and (ii) calculating Equation (3) increasing the bandwidth. Then, to evaluate the impact of the rotation angle of the transmitter for artefact removal, the procedure was repeated using two transmitting positions displaced 5° (i.e., transmitting $\Delta\phi = 5^\circ$) and using two transmitting positions displaced 10° (i.e., transmitting $\Delta\phi = 10^\circ$).

3. Results and Discussions

The authors in [18] performed a study for bone imaging, collecting the signals in multi-monostatic fashion and using antennas immersed in a coupling liquid. In [18], imaging was performed using a beamforming procedure named non-coherent migration, after applying an average trace subtraction strategy to remove the artefact. Instead, here, we collect the signals in multi-bistatic fashion, using antennas in free space; imaging was performed using an HP based algorithm, which operated in the frequency domain, after applying a rotation subtraction strategy to remove the artefact.

It may happen that artefact removal is not effective to cancel the artefact fully, partially or completely masking the inclusion, i.e., the lesion. This may be due to imperfect cancellation of the transmitting antenna or appropriate cancellation of the first layers' reflection or even due to multiple reflections occurring inside the phantom that cannot cancel completely. Figures 6 and 7 show all the images of the experimental phantom investigated in various frequencies and various bandwidths for bone marrow lesion and bone fracture scenarios, respectively. The correct position of the lesion is indicated by the arrow. The left columns refer to artefact removal performed using a transmitting step $\Delta\phi = 5^\circ$, while the right columns refer to artefact removal performed using a transmitting step $\Delta\phi = 10^\circ$.

It is important to point out that all the images shown here were normalized and adjusted, forcing the intensity values below 0.5 to zero. However, SCR was calculated before performing the image adjustment.

As Figures 6a,b and 7a,b show, in the frequency range from 1 GHz to 1.5 GHz, the artefact masked the inclusion. When using the frequency range from 1.5 GHz to 2 GHz (see Figures 6c,d and 7c,d) and from 2 GHz to 2.5 GHz (see Figures 6e,f and 7e,f), only the lesion was visible, without any residual clutter. Images corresponding to a frequency range of 2.5 GHz to 3 GHz depicted that, although the lesion was detectable, the presence of residual clutters could not be ignored (see Figures 6g,h and 7g,h).

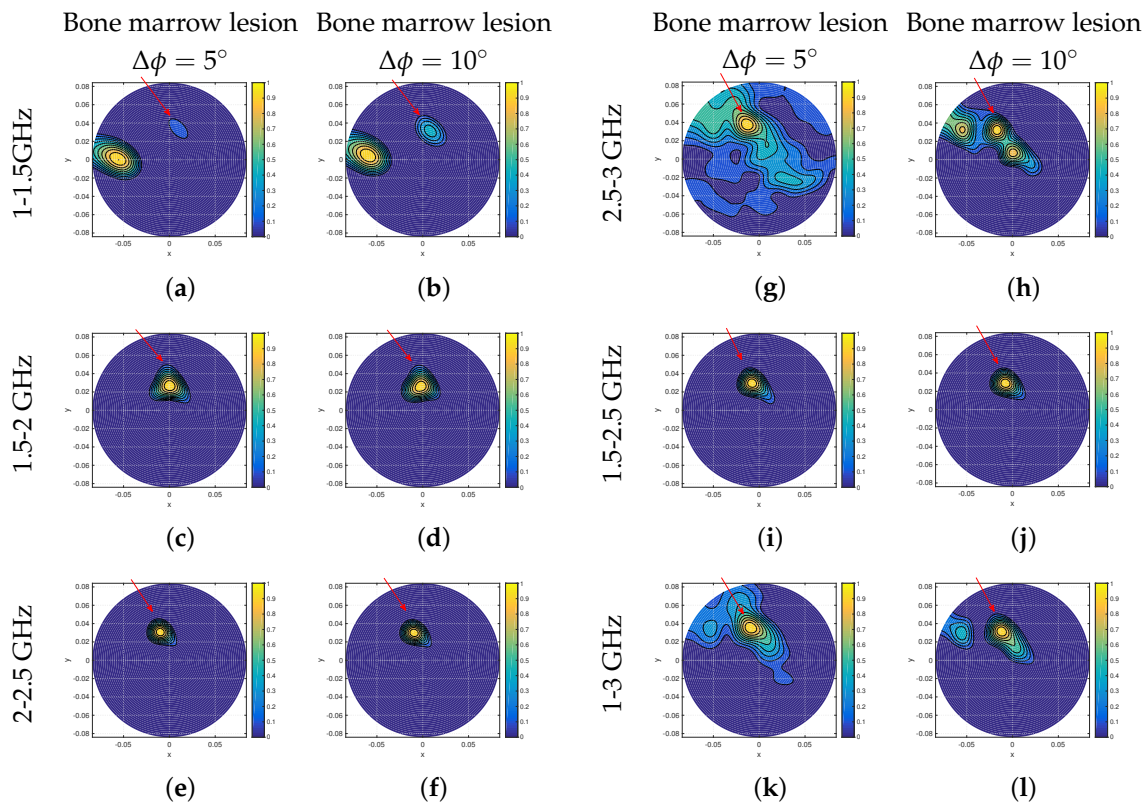


Figure 6. Microwave images of the bone marrow lesion employing various frequencies and bandwidths; (a,b), (c,d), (e,f) and (g,h) represent the resulting images when employing frequency ranges 1–1.5 GHz, 1.5–2 GHz, 2–2.5 GHz and 2.5–3 GHz, respectively, while (i,j) and (k,l) represent the images when considering bandwidth equal to 1 GHz and 2 GHz, respectively. Images are obtained following normalization to their correspondent maximum values and forcing to zero the intensity values below 0.5 (X and Y are given in meters).

After visual inspection, image quantification was performed calculating the resolution and SCR. Table 3 summarises such parameters.

Table 3. Resolution (m) and SCR (linear) for various frequency ranges.

Frequency GHz	Bone Marrow Lesion				Bone Fracture			
	$\Delta\phi = 5^\circ$		$\Delta\phi = 10^\circ$		$\Delta\phi = 5^\circ$		$\Delta\phi = 10^\circ$	
	Resolution, m	SCR	Resolution, m	SCR	Resolution, m	SCR	Resolution, m	SCR
1–1.5	N/A	<1	N/A	<1	N/A	<1	N/A	<1
1.5–2	0.015	2.06	0.015	2.13	0.016	1.85	0.016	1.51
2–2.5	0.012	2.13	0.012	1.88	0.011	2.09	0.011	1.92
2.5–3	0.017	1.38	0.015	1.52	N/A	<1	N/A	<1

Concerning the bone marrow lesion, as Table 3 shows, the highest SCR values were related to the frequency ranges from 1.5 GHz to 2 GHz and from 2 GHz to 2.5 GHz. The same holds for the bone fracture scenarios. Concerning resolution, resolutions of 1.2 cm and of 1.1 cm were achieved for the bone marrow lesion and bone fracture, respectively, when employing a frequency range from 2 GHz to 2.5 GHz. The result of operating frequency range from 2.5 GHz to 3 GHz showed that a further increase of the central frequency did not imply high SCR and/or better resolution, since residual clutter may be enhanced.

Turning now to investigate the impact of increasing the bandwidth, SCR and resolution values were calculated employing a frequency from 1.5 GHz to 2.5 GHz (i.e., a bandwidth of 1 GHz) and a

frequency from 1 GHz to 3 GHz (i.e., a bandwidth of 2 GHz). As Table 4 shows, the highest SCR (2.22) corresponded to the bandwidth of 1 GHz compared to employing a bandwidth of 2 GHz (SCR = 1.49). It was evident that, although increasing the bandwidth of operation might be beneficial for SCR [28], such a bandwidth increase should be performed carefully to avoid including a region of frequency where residual clutter may be enhanced.

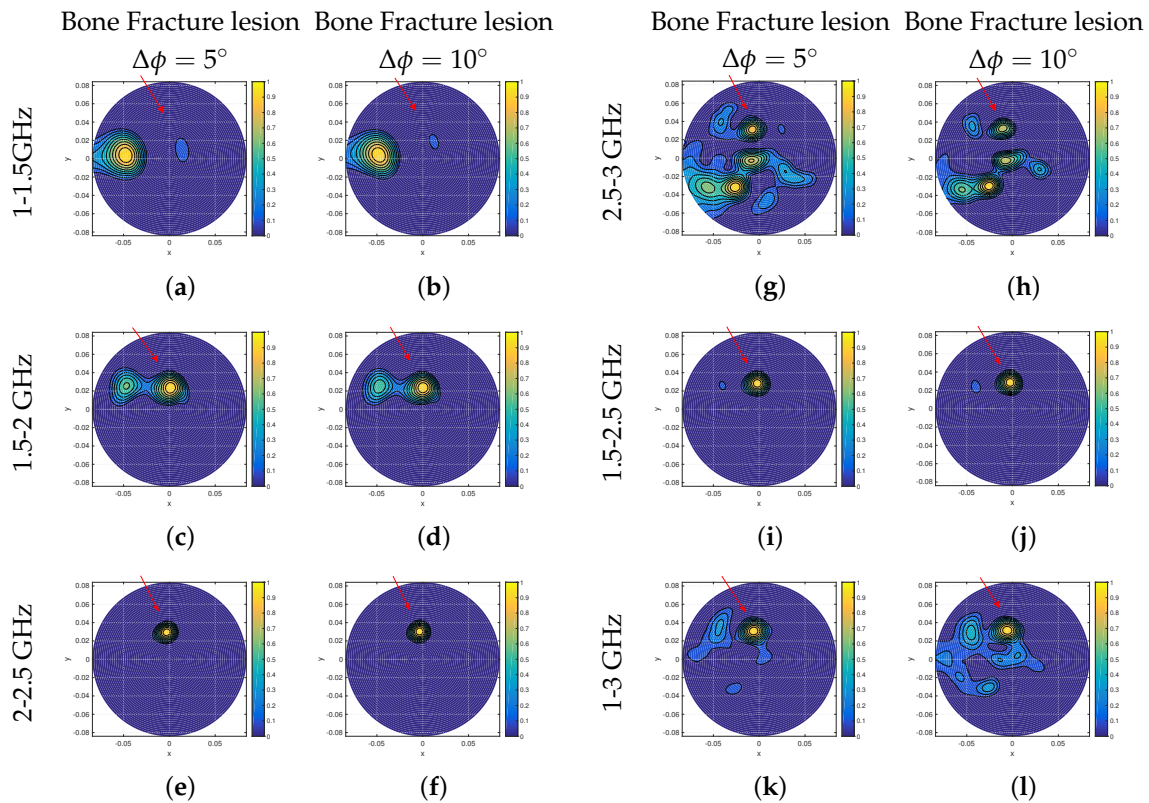


Figure 7. Microwave images of the bone fracture lesion employing various frequencies and bandwidths; (a,b), (c,d), (e,f) and (g,h) represent the resulting images when employing frequency ranges 1–1.5 GHz, 1.5–2 GHz, 2–2.5 GHz and 2.5–3 GHz, respectively, while (i,j) and (k,l) represent the images when considering bandwidth equal to 1 GHz and 2 GHz, respectively. Images are obtained following normalization to their correspondent maximum values and forcing to zero the intensity values below 0.5 (X and Y are given in meters).

Table 4. Resolution (m) and SCR (linear) for various bandwidths.

Bandwidth GHz	Bone Marrow Lesion				Bone Fracture			
	$\Delta\phi = 5^\circ$		$\Delta\phi = 10^\circ$		$\Delta\phi = 5^\circ$		$\Delta\phi = 10^\circ$	
	Resolution, m	SCR	Resolution, m	SCR	Resolution, m	SCR	Resolution, m	SCR
1.5–2.5	0.013	2.22	0.014	2.06	0.011	1.78	0.012	1.74
1–3	0.018	1.49	0.015	1.34	0.013	1.51	0.013	1.36

A further confirmation of such a finding may be drawn through a visual inspection of Figures 6i,j and 7i,j and Figures 6k,l and 7k,l, which show the images employing the bandwidth of 1 and 2 GHz for both the bone marrow lesion and bone fracture, respectively.

The highest value of SCR, which was equal to 2.22, was obtained through the HP procedure using a bandwidth of 1 GHz (1.5 GHz to 2.5 GHz). It should be emphasized that our obtained linear value of SCR 2.22 corresponded to 6.9 dB, which was in excellent agreement with [28,29]. According to Table 3, the resolution that came from the experiments (1.1 cm) was in excellent agreement with the optical resolution limit of $\lambda_{1,f_{max}}/4$, where $\lambda_{1,f_{max}}$ represents the wavelength in the scenarios by

considering a dielectric constant equal to the arithmetical average of the two layers calculated at the highest frequency of 3 GHz [28,29].

Concerning the impact of the transmitter $\Delta\phi$ in artefact removal, we observed that for a large lesion size (radius = 0.7 cm), similar SCR values were obtained when using both $\Delta\phi = 5^\circ$ and 10° . Instead, for a small lesion size (radius = 0.3 cm), SCR obtained when using $\Delta\phi = 5^\circ$ was higher than that obtained for 10° . It is worthwhile pointing out that $\Delta\phi = 5^\circ$ corresponded to a spatial displacement of 0.87 cm, while $\Delta\phi = 10^\circ$ corresponded to a spatial displacement of 1.74 cm. Thus, we may conclude that optimal artefact removal was obtained with a transmitting $\Delta\phi = 5^\circ$, leading to a spatial displacement approximately of the same magnitude as the dimension of the lesion.

4. Conclusions

This paper presented the application of a new radar based microwave imaging procedure based on the Huygens principle approach, which achieved promising results for bone lesion detection. The procedure was successfully tested inside an anechoic chamber on a dedicated multilayer phantom. Subtraction between S21 obtained using two transmitting positions was employed in order to remove the artefact. The quantification of the microwave images was calculated using two parameters, which were the resolution and SCR, achieving an SCR of 2.22 and a resolution of 1.1 cm when using a frequency range from 1.5 GHz to 2.5 GHz. A further bandwidth increase may lead to an enhancement of the residual clutter.

It should be empathized that S21 is a measure of the total field; thus, detection can be achieved only after artefact removal, which can cancel the image of the transmitter and the reflection of the first layers. Together with the subtraction between S21 obtained using two slightly displaced transmitting positions, i.e., rotation subtraction, there are also other techniques that may be used for artefact removal, both in the frequency and in time domain [30]. Among the techniques in the frequency domain, the rotation subtraction could be effective also for imaging highly asymmetric scenarios (such as human bones), since it assumes only the similarity of the first layers' reflection when displacing slightly the transmitting position.

Research is in progress to show the performance of the procedure in case of multiple fractures, investigating the impact of zeroing all intensity values below 0.5 in the detection of real defects. Moreover, a comparison of the performances between rotation subtraction artefact removal and (local) average subtraction artefact removal is also in progress.

Ultimately, this paper verified that the microwave scanning procedure, which was based on HP, can be used to perform bone imaging to detect lesions and fractures in bone layers successfully, negating the use of X-rays. Our proposed scanning procedure was simple and required only two antennas in free space, thus no matching liquid was needed. This paper may pave the way for the construction of a dedicated bone imaging system that is inexpensive, compact, and portable, since it resorts to two rotating antennas coupled through a VNA.

Author Contributions: Conceptualization, B.K., M.G. and G.T.; methodology, B.K., B.S., N.G. and G.T.; supervision, M.G. and S.D.; validation, B.K., B.S., N.G., M.G., S.D. and G.T.; writing, original draft preparation, B.K. and N.G.; writing, review and editing, M.G., S.D. and G.T.

Funding: The project leading to this application received funding from the European Union's Horizon 2020 research and innovation programme under the Marie Skłodowska-Curie Grant Agreement No. 793449.

Conflicts of Interest: The authors declare no conflict of interest.

References

1. Oryan, A.; Monazzah, S.; Bigham- Sadegh, A. Bone Injury and Fracture Healing Biology. *Elsevier Biomed. Environ. Sci.* **2018**, *28*, 57–71.
2. Meaney, P.M.; Goodwin, D.; Golnabi, A.; Pallone, S.; Geimer, A.; Paulsen, K.D. 3D Microwave bone imaging. In Proceedings of the 6th European Conference on Antennas and Propagation (EUCAP), Prague, Czech Republic, 26–30 March 2012; pp. 1770–1771. [[CrossRef](#)]

3. Pham, D.L.; Xu, C.; Prince, J.L. Current methods in medical image segmentation. *Annu. Rev. Biomed. Eng.* **2000**, *2*, 315–337. [PubMed]
4. Al Nahid, A.; Khan, T.M.; Kong, Y. Hardware Implementation of Bone Fracture Detector Using Fuzzy Method Along with Local Normalization Technique. *Ann. Data Sci.* **2017**, *4*, 533–546. [CrossRef]
5. Mercuri, M.; Sheth, T.; Natarajan, M. Radiation exposure from medical imaging: A silent harm? *CMAJ* **2011**, *183*, 413–414. [CrossRef] [PubMed]
6. Kak, A.C.; Slaney, M. *Principle of Computerized Tomography*; IEEE Free Press: New York, NY, USA, 1987.
7. Staderini, E.M. UWB radars in medicine. *IEEE Aerosp. Electron. Syst. Mag.* **2002**, *17*, 13–18. [CrossRef]
8. Joines, W.T.; Jirtle, R.L.; Rafal, M.D.; Schaefer, D.J. Microwave power absorption differences between normal and malignant tissue. *Int. J. Rad. Oncol. Biol. Phys.* **1980**, *6*, 681–687. [CrossRef]
9. Meaney, P.M.; Paulsen, K.D. Nonactive antenna compensation for fixed-array microwave imaging: Part II imaging results. *IEEE Trans. Med. Imag.* **1980**, *18*, 508–518. [CrossRef]
10. Winters, D.W.; Van Veen, B.D.; Hagness, S.C. A sparsity regularization approach to the electromagnetic inverse scattering problem. *IEEE Trans. Antennas Propag.* **2010**, *158*, 145–154. [CrossRef]
11. Li, X.; Bond, E.J.; Van Veen, B.D.; Hagness, S.C. An overview of ultra-wideband microwave imaging via space-time beamforming for early-stage breast-cancer detection. *IEEE Antennas Propag. Mag.* **2005**, *47*, 19–34.
12. Porter, F.; Kirshin, E.; Santorelli, A.; Coates, M.; Popović, M. Time-domain multistatic radar system for microwave breast screening. *IEEE Antennas Wirel. Propag. Lett.* **2013**, *12*, 229–232. [CrossRef]
13. Santorelli, A.; Porter, E.; Kang, E.; Piske, T.; Popović, M.; Schwartz, J.D. A time-domain microwave system for breast cancer detection using a flexible circuit board. *IEEE Trans. Instrum. Meas.* **2015**, *64*, 2986–2994. [CrossRef]
14. Nikolova, A. Microwave imaging for breast cancer. *IEEE Microw. Mag.* **2011**, *12*, 78–94. [CrossRef]
15. Semenov, S.Y.; Corfield, D.R. Microwave tomography for brain imaging: Feasibility assessment for stroke detection. *Int. J. Antenna Propag.* **2008**, *2008*, 254830. [CrossRef]
16. Porter, E.; Coates, M.; Popović, M. An early clinical study of time-domain microwave radar for breast health monitoring. *IEEE Trans. Biomed. Eng.* **2016**, *63*, 530–539. [CrossRef]
17. Salvador, S.M.; Fear, E.C.; Okoniewski, M.; Matyas, J.R. Exploring joint tissues with microwave imaging. *IEEE Trans. Microw. Theory Tech.* **2010**, *58*, 2307–2313. [CrossRef]
18. Ruvio, G.; Cuccaro, A.; Solimene, R.; Brancaccio, A.; Basile, B.; Ammann, M.J. Microwave bone imaging: A preliminary scanning system for proof-of-concept. *Healthc. Technol. Lett.* **2016**, *3*, 218–221. [CrossRef]
19. Mirbeik-Sabzevari, A.; Tavassolian, N. Tumor Detection Using Millimeter-Wave Technology: Differentiating Between Benign Lesions and Cancer Tissues. *IEEE Microw. Mag.* **2019**, *20*, 30–43. [CrossRef]
20. Gabriel, C.; Gabriel, S.; Corthout, E. The dielectric properties of biological tissues: I. literature survey. *Phys. Med. Biol.* **1996**, *41*, 2231–2249. [CrossRef]
21. Zurich Med Tech. 2019. Available online: <https://zmt.swiss/validation-hw/tsm/tle5c-24-2450/> (accessed on 26 October 2019).
22. Meaney, P.M.; Fox, C.J.; Geimer, S.D.; Paulsen, K.D. Electrical Characterization of Glycerin: Water Mixtures: Implications for Use as a Coupling Medium in Microwave Tomography. *IEEE Trans. Microw. Theory Tech.* **2017**, *65*, 1471–1478. [CrossRef]
23. Sani, L.; Paoli, M.; Raspa, G.; Ghavami, N.; Sacchetti, F.; Saracini, A.; Ercolani, S.; Vannini, E.; Duranti, M. Initial Clinical Validation of a Novel Microwave Apparatus for Testing Breast Integrity. In Proceedings of the IEEE International Conference on Imaging Systems and Techniques (IST), Chania, Greece, 4–6 October 2016; pp. 278–282. [CrossRef]
24. Tiberi, G.; Ghavami, N.; Edwards, D.J.; Monorchio, A. Ultrawideband microwave imaging of cylindrical objects with inclusions. *IET Microw. Antennas Propag.* **2011**, *5*, 1440–1446. [CrossRef]
25. Enders, P. Huygens' principle as universal model of propagation. *Latin Am. J. Phys. Educ.* **2009**, *3*, 19–32.
26. Sani, L.; Ghavami, N.; Vispa, A.; Paoli, M.; Raspa, G.; Ghavami, N.; Sacchetti, F.; Vannini, E.; Ercolani, S.; Saracini, A.; et al. Novel microwave apparatus for breast lesions detection: Preliminary clinical results. *Biomed. Signal Process. Control* **2019**, *52*, 257–263.
27. Ghavami, N.; Tiberi, G.; Edwards, D.J.; Safaai-Jazi, A.; Monorchio, A. Huygens principle based imaging of multilayered objects with inclusion. *Prog. Electromagn. Res.* **2014**, *58*, 139–149.
28. Ghavami, N.; Tiberi, G.; Edwards, D.J.; Monorchio, A. UWB Microwave Imaging of Objects with Canonical Shape. *IEEE Trans. Antennas Propag.* **2012**, *60*, 231–239. [CrossRef]

29. Fear, E.C.; Li, X.; Hagness, S.C.; Stuchly, M.A. Confocal microwave imaging for breast cancer detection: Localization of tumors in three dimensions. *IEEE Trans. Biomed. Eng.* **2002**, *4*, 812–822.
30. Elahi, M.A.; Glavin, M.; Jones, E.; O' Halloran, M. Artifact Removal Algorithms for Microwave Imaging of the Breast. *Prog. Electromagn. Res.* **2013**, *141*, 185–200. [[CrossRef](#)]



© 2019 by the authors. Licensee MDPI, Basel, Switzerland. This article is an open access article distributed under the terms and conditions of the Creative Commons Attribution (CC BY) license (<http://creativecommons.org/licenses/by/4.0/>).